UC Santa Cruz
UC Santa Cruz Electronic Theses and Dissertations

Title

ARPES Study of the Topological Insulator Bi2Se3

Permalink

https://escholarship.org/uc/item/28v003zp

Author

Kim, Ahram

Publication Date

2015

Peer reviewed|Thesis/dissertation

UNIVERSITY OF CALIFORNIA

SANTA CRUZ

ARPES Study of the 3D Topological Insulator Bi$_2$Se$_3$

A thesis submitted in partial satisfaction
of the requirements for the degree of

MASTER OF SCIENCE

in

PHYSICS

by

Ahram Kim

December 2015

The Thesis of Ahram Kim
is approved:

_____

Gey-Hong Gweon, Ph.D.

_____

Professor Sue Carter

_____

Professor Alexander Sher

_____

Tyrus Miller
Vice Provost and Dean of Graduate Studies

Table of Contents

List of Figures

Abstract

ARPES Study of the 3D Topological Insulator Bi_2Se_3

by

Ahram Kim

The 3D topological insulator material Bi_2Se_3 is characterized with angle-resolved photoemission spectroscopy (ARPES) energy-momentum intensity spectra at various temperatures. High quality samples with relatively small band gaps and a low energy Dirac point were used. An ideal resolution was determined to be taken at photon energy of 11eV. Scattering interaction at the surface can come from three main sources: electron-phonon, surface impurity, or electron-electron scattering, between the surface and the bulk conduction bands. Momemtum- and Energy- Distribution Curves (MDC and EDC) fits were modeled with Gaussian convoluted Lorentzian and extremely-correlated Fermi liquid theory, respectively. By comparing the binding energy at different temperatures for regions near the Fermi edge and near the Dirac point, and observing an increase in MDC self-energy near the Fermi edge, we conclude that a source of interaction is through phonon coupling channels. By calculating the coupling constant λ from self-energy at various temperatures, we present a very low value of $\lambda = 0.049 \pm 0.007$ which supports our conclusion that phonon coupling must be incorporated into the theory to provide accurate fit models. Data was taken at beam line 5-4 at the Stanford Synchrotron Radiation Lightsource in Menlo Park, with samples prepared by Genda Gu's group at Brookhaven National Laboratory.

Dedication.

Dedicated and devoted.

Acknowledgements.

In acknowledgement are all the persons

1 Introduction

Based on the photoelectric effect, photoelectric spectroscopy is a class of exper-
imental probing techniques that lend themselves ideally to the direct mapping
of the electronic structures in materials– particularly those exhibiting 2D or
surface-state phenomena, such as topological insulators. Angle-resolved photo-
electric spectroscopy (ARPES) maps emission data directly in momentum and
energy. For materials with negligible dependence on k_z, the ability to image
the electronic band structure as it depends on crystal momentum simplifies
the process of finding the dispersion relation of the material. The surface state
nature of topological insulators is additionally beneficial to ARPES due to the
methods dependence on the photoelectrons mean free path, which is limited to
around 5 Å for a typical beamline photon energy of 7 to 40 eV [12]. It should
be noted that the limitation can be lessened by working in ultra-high vacuum
($< 5 \times 10^{-11}$ torr), with in-situ cleaving of the sample surface.

1.1 Mechanics of ARPES

Described by Heinrich Hertz in 1887 and defined by Albert Einstein in 1905
[13, 8], the photoelectric effect arises from the quantum nature of light and
the parceling of its energy into distinct quanta called photons. As well as sig-
nificant theoretical advances, the photoelectric effect has also facilitated the
development of more and better experimental techniques for the study of ma-
terials. Photoemission (or photoelectric) spectroscopy is a tool for studying
the electron band occupancy of materials. With the advent of high intensity
synchrotron radiation sources in the 1960's and the improvement of electron
energy analyzers, photoemission techniques quickly became a thriving field of
research and development. ARPES is an angularly resolved form of photoemis-
sion spectroscopy which is particularly ideal for the study of the momentum

dependence of a band structure in quasi-low dimensional materials. Here, quasi-low dimensional refers to 3D crystal structures composed of adjacent 2D planes with correlated electron behavior which are electronically anisotropic near the Fermi energy.

When electromagnetic radiation is incident on a material, the valence electrons of its atoms can absorb the energy of the incoming photons and be ejected from the material. The resultant kinetic energy of these photoelectrons is the energy of the absorbed photon, less the electrons binding energy E_B and the energy lost to the surface potential barrier ϕ :

$$E_{kin} = h\nu - \phi - |E_B| \tag{1}$$

$$p_{||} = \hbar k_{||} = sin\theta(2mE_{kin})^{1/2} \tag{2}$$

A schematic representation of the ARPES energetics is shown in Figure 1. Photons from a synchrotron radiation source is incident upon a sample surface oriented perpendicular to the plane of photon propagation. The intensity and kinetic energy of the photoelectrons are measured by an electron energy analyzer, which captures photoelectrons within a resolution cone at a location (θ, ϕ) from the surface normal. Variable experimental parameters include incident energy, angle, and polarization of the photon, and exit angles, kinetic energy, electron spin of the photoelectron, and the temperature T of the sample and the chamber. The intensity recorded by the electron analyzer can potentially be a function of all of these variables; however, in order to simplify the experiment, most of the variables are integrated over or kept constant. [12, 28] The electric link between the sample and the spectrometer sets the chemical potential μ of both to be equal (where μ is also the Fermi energy E_F of the sample). The potential barrier ϕ_{sample} is not necessarily known for all samples, but ϕ_{spectr} can be measured against a well known material; in this experiment,
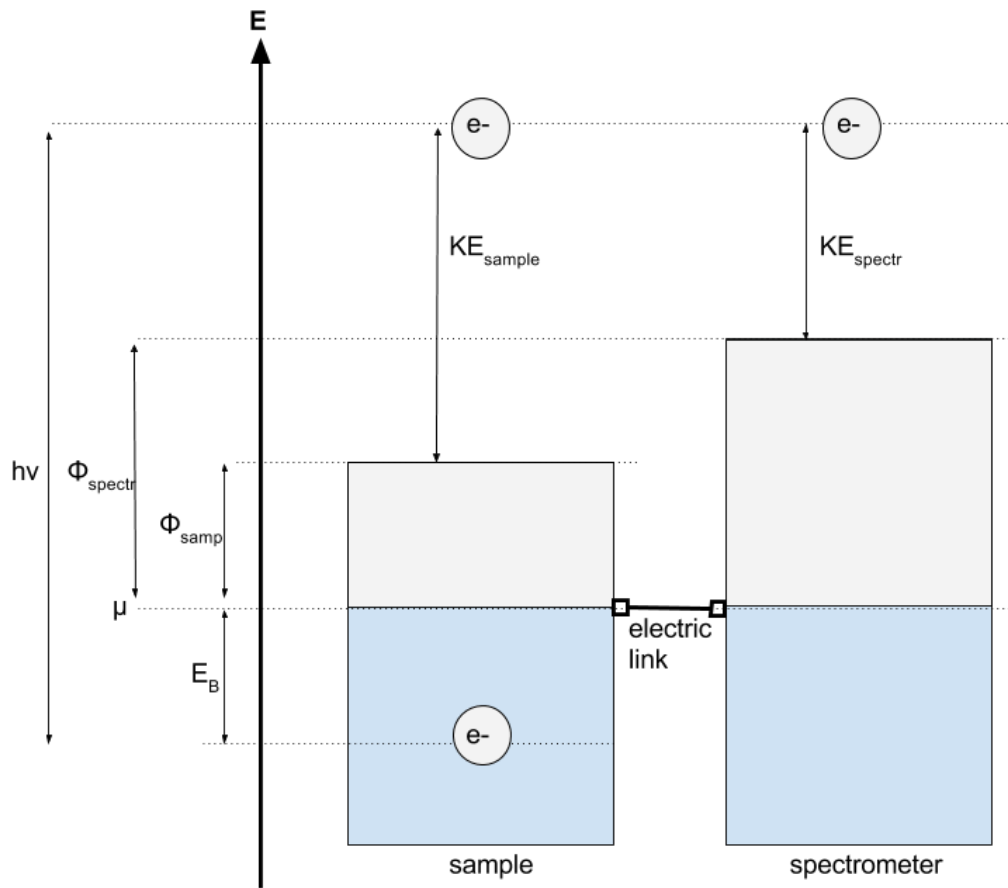
Figure 1: Schematic photoelectric effect energetics of a spectrometer. The final kinetic energy of a photoelectron is the incident photon energy $h\nu$ less the binding energy E_B and the potential barrier ϕ at the surface. Adjustment must be made to account for the difference in ϕ_{sample} and ϕ_{spectr} when calculating the samples E_B. Adapted from G.-H. Gweon's Ph.D. thesis. [12]

an edge was estimated from the low temperature spectra taken at 25K, as a gold spectra was not taken. From the known incoming photon energy, the binding energy E_B of the sample can be determined; here, a shift of 6.4 eV was extracted from the fit, shown laterin Fig.9.
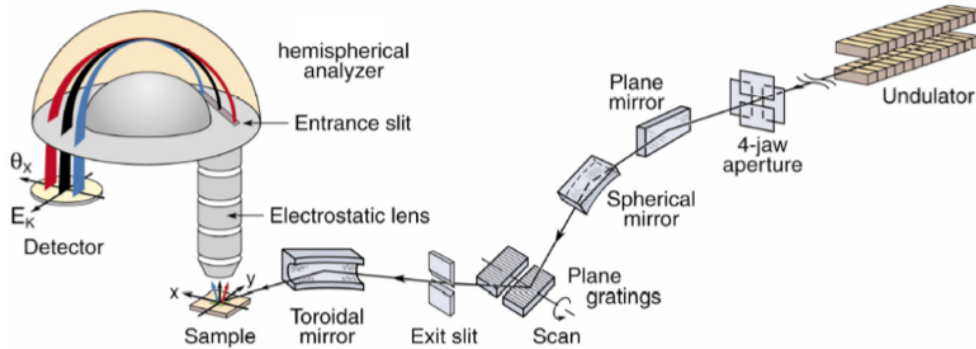
Figure 2: Diagram of a synchrotron undulatory and ARPES hemispherical analyzer setup. From G.-H. Gweon's Ph.D. thesis.[12]

The photodetector lies at one end of a hemispherical analyzer which gathers the photoelectrons ejected from a sample which is hit with photons produced by an undulator leg of a synchrotron light source. [8] A representative diagram of the setup is shown in Figure 2. [7]

Data for this work was taken at beamline 5-4 at the Stanford Synchrotron Radiation Lightsource (SSRL) at SLAC in Menlo P, CA. The hemispherical analyzer used here is SCIENTA R4000 Electron Analyzer, and the optimal energy and momentum resolution range (0.1deg) was obtained at a photon energy of 11 eV, from an available range between 7 and 25 eV. Once at the hemispherical analyzer, the photoelectron signal is amplified and focused onto a charge coupled device (CCD) for detection.

The hemispherical analyzer is detailed further in Figure 3. Two metal hemispheres with a potential difference separates collected photoelectrons according to their exit kinetic energy and momenta. A micro-channel plate at the de-
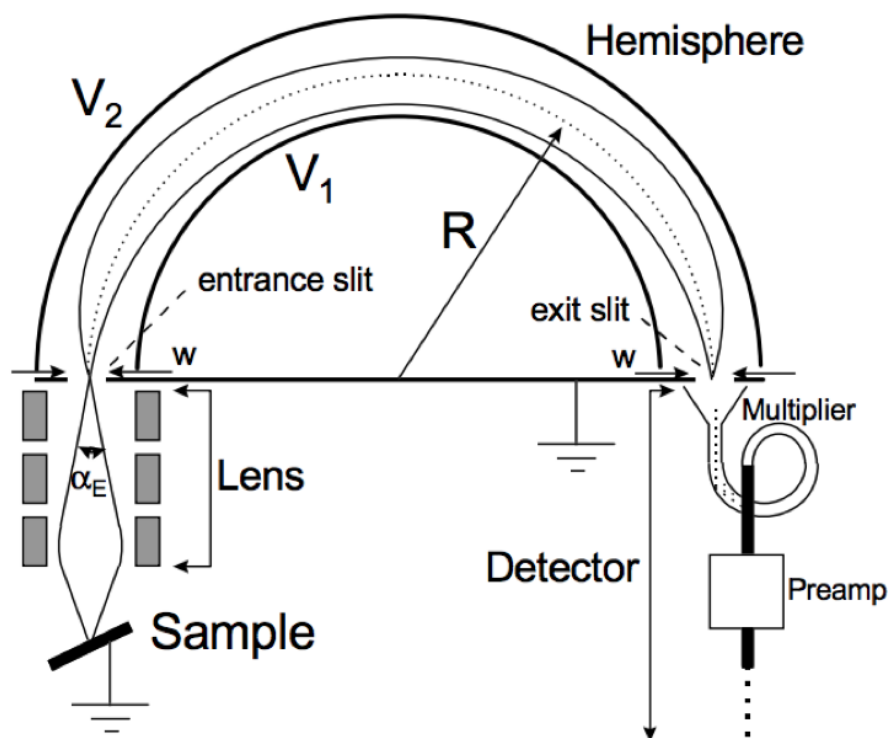
Figure 3: The hermispherical analyzer. Photoelectrons from a sample is focused and herded between charged hemispheres to an exit slit before being amplified for detection. From G.-H. Gweon's Ph.D. thesis.[12]

tector end amplifies the signal and transfers the electron beam to a phosphor screen which emits the signal as photons. The CCD then collects the photons into energy and momentum bins to produce 2D intensity slices; stacked together, these slices can create a 3D movie of the electron density for momentum, i.e. angular, position at a range of binding energies.

The energy and direction of a range of these photoelectrons can then be measured, and the parallel (to surface) component of the crystal momentum calculated by Eq.2, where θ is the polar angle of emission. Perpendicular components of momentum are not considered here due to the lack of translational symmetry along the direction normal to the surface.

The shallow probe depth ($\sim 10\mathring{A}$) of low-energy PES is a double-edged sword: on one hand, it allows for higher resolution in band structure mapping, but it also makes data vulnerable to significant degradation from surface collisions in an inevitably imperfect vacuum. As such, precautions must be taken to reduce the effect of surface contamination on the data collected. In order to preserve the surface integrity of the sample for as long as possible, the sample is cleaved to reveal a fresh experimental surface once it is moved into the high vacuum chamber. To do this, a post is glued normal to the sample face and knocked off with magnetic arms in the chamber. The vacuum is kept around $5x10^{-11}$ Torr.

A simple derivation of the electrons momentum inside a sample can be done using the conservation of momentum and the measured momentum of the ejected photoelectron. An ejected photoelectron (that is, the data which is captured by the photoanalyzer at a beamline setup) can be approximated to be a free electron traveling in vacuum. The energy-momentum dispersion relation of a free electron is known:

$$E_{kin} = \frac{(\hbar k)^2}{2m} \tag{3}$$

6
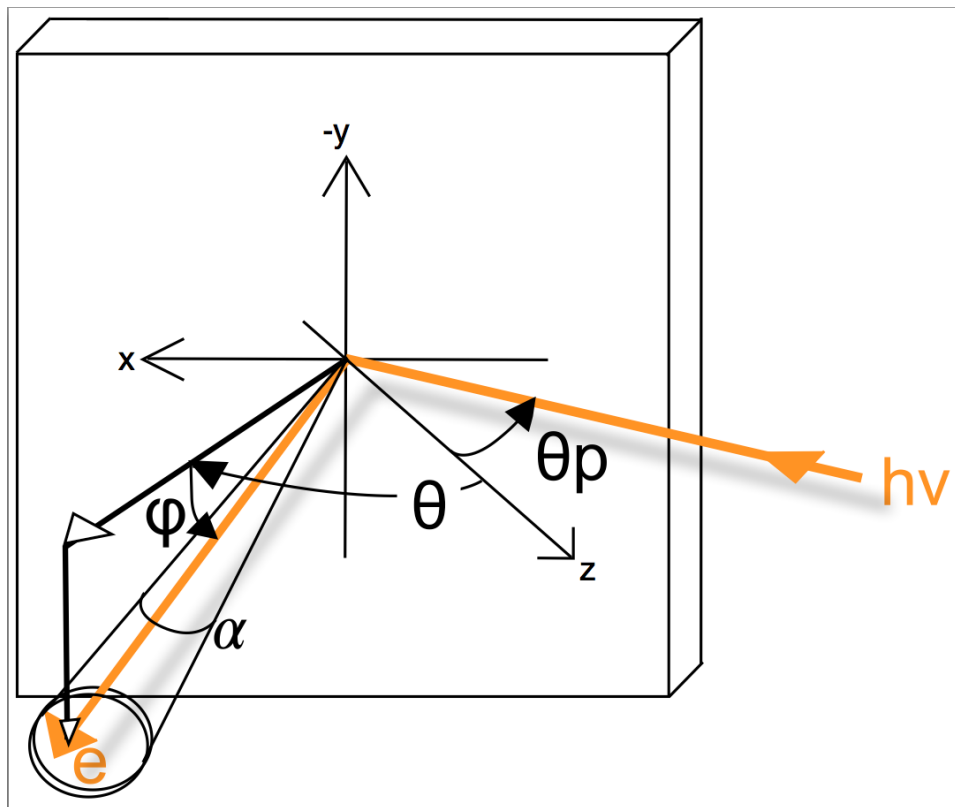
Figure 4: Exit and entrance angles of photoelectrons and incident photon beam. Adapted from [12].

or:

$$k = \frac{(2mE_{kin})^{1/2}}{\hbar} \tag{4}$$

Using $m = m_e = \frac{0.511 \times 10^6}{3 \times 10^{18}}$ $[\frac{eV \cdot s^2}{\mathring{A}^2}]$ and $\hbar = 6.582 \times 10^{-16}$ [eV·s], the expression for **k** simplifies to:

$$k = 0.512(E_{kin})^{1/2} \tag{5}$$

with units in $[1/\mathring{A}]$ for momentum, and E_{kin} in [eV]. This **k** is a vector, which can then be broken down into its x-, y-, and z- components using the polar angle θ and the azimuthal angle ϕ as shown in Fig.4:

$$\left. \begin{aligned} k_{x,out} &= 0.512\sqrt{E_k}\cos\phi\sin\theta \\ k_{y,out} &= 0.512\sqrt{E_k}\sin\phi \\ k_{z,out} &= 0.512\sqrt{E_k}\cos\phi\cos\theta \end{aligned} \right\} \tag{6}$$

The separation of **k** into components allows the unconserved z-component to be adjusted separately, while the conservation of momentum in the periodic crystal is applied to the x- and y- directions defining the parallel plane to the surface. For the z-direction, a simplified, step-potential V_0 is applied to compensate for the diffraction of momentum at the boundary. This inner potential V_0, is defined to be negative inside the material and drops to 0 at the surface. Taking these approximations, the momentum components inside the crystal can be derived:

$$\left. \begin{aligned} k_{x,in} &= k_{x,out} \\ k_{y,in} &= k_{y,out} \\ k_{z,in} &= \sqrt{k_{z,out}^2 + 0.512^2 V_0} \end{aligned} \right\} \tag{7}$$

8

1.2 Approximations Taken in the Experimental Setup

The general photoelectron intensity equation described previously must have a few adjustments made to apply it to ARPES data. [12]

The first is to integrate the expression over an entire single band. Further, restrictions from the experimental resolution (here, in energy and momentum) must be applied for the monochromator and the electron analyzer being used. These two steps are combined into one step by adding resolution functions to the integral. The energy resolution function W_W can be determined from a reference spectrum of a well-known material such as gold. Momentum resolution comes from the angular limits of the dispersion relations $\epsilon(k)$ determined earlier in this chapter.. However, the momentum resolution function $W_k = W(\epsilon(k))$ is more complicated and requires some simplifying assumptions.

1. The material has no z-dependence in its electron-momentum relation due to its low-dimensional electron structure- i.e. the surface state nature for TBI. ARPES measurements are taken along a single, in-plane axis of the crystal surface (Fig.4). This assumption is used to make further assumptions. Also, this means for 2D crystals (or rather TBI with weakly interacting 2D layers), determination of the inner potential is not crucial.

2. The incident photon beam is completely sharp; since the momentum resolution depends on the dispersion relations whose components depend on α and θ defining the angle cone of Fig.4, the incident spot must be perfectly sharp to maintain the small, minimum value of the angle cone. The small angle approximation applied to Eq.9 gives a linear relation between angle- and momentum- space. Approximations allow the range of integration for k to be specified along the 2 in-plane directions. We

get, for $W(\epsilon(\text{k}))$:

$$W_\epsilon(\epsilon') \propto \frac{1}{\epsilon_2 - \epsilon_1} \sqrt{1 - \frac{4(\epsilon' - \epsilon(\mathbf{k}))^2}{(\epsilon_1 - \epsilon_1)^2}} \tag{8}$$

3. The unavoidable broadening of the resolution function must be acknowledged, particularly when working with k near k_F; the broadening results in a tail in the resolution function, so a fit line with a tail is preferred– such as a Gaussian rather than the elliptical function defined above.

4. The finite photoelectron lifetime must be accounted for, by integrating the imaginary part of the Green function over the perpendicular k range as well as those parallel to the surface. This integration would be a density function along the perpendicular direction if the range is on the order of one Brillouin zone height. This effect is small for 2 dimensional materials like TBI.

5. Experimental misalignment of the sample, away from the ideal perpendicular alignment of the crystal surface to the photon beam, is adjusted by adding a new set of axis along the analyzers mount. The photoelectron analyzer axis is defined to be the new point of measurement for θ and ϕ. The relative angles to the sample normal is defined to be ϕ_{normal} and a trivial rotation renormalization for θ. Small angle assumption is maintained. The momentum relations Eq. 9 are now redefined:

$$\left.\begin{aligned}
k_{x,out} &= 0.512\sqrt{E_k}\cos\phi\sin\theta \\[2mm]
k_{y,out} &= 0.512\sqrt{E_k}(\sin\phi\cos\phi_N - \cos\phi\cos\theta\sin\phi_N) \\[2mm]
k_{z,out} &= 0.512\sqrt{E_k}(\sin\phi\sin\phi_N + \cos\phi\cos\theta\cos\phi_N)
\end{aligned}\right\} \tag{9}$$

1.3 Approximations Taken in the Formalism

The formalism of photoemission, which is used to analyze ARPES data, takes a couple of significant approximations for the sake of simplification. A more correct approximation would work in the quantum mechanical framework, which the three-step model discussed later on does not incorporate ideally. This approach would be a one-step model of photoemission which includes a single hamiltonian of the entire system involved in the collection of a photoelectron: bulk, surface, and vacuum. Instead of three independent steps, there is an initial and final wavefunction which obeys specific boundary conditions at the surface of the material. An overlap between the initial and final states allow for the emission of a photoelectron. Energy and momentum conservation laws are also applied to the photon and bulk electron system. However, the many-body wave functions are difficult to work with; and since the complexity of such a system is not necessary to sufficiently describe the process, simplification is taken through the sudden approximation. This approximation removes many-body interactions and relaxation during photoemission. [5, 18]

1.4 The Three-Step Model and Sudden Approximation

The equations describing the energetics of photoelectron emission in ARPES can be described in three steps, known as the *three-step model*. [27, 2, 9, 26] Three sequential steps are addressed in independent steps:

(i) the excitation of the bulk electron by a photon ($\sim h\nu$)

(ii) electron transport from the bulk to the surface ($\sim E_B$)

(iii) electron transport from the surface to the vacuum ($\sim \phi_{sample}$)

The assumption made in the three-step model is that the momentum from

initial to final state is approximately conserved. Because the momentum of the incident photon is much less than that of the ejected photoelectron, momentum loss can be negligible. This model is particularly applicable to 2D systems.

A different approach is the sudden approximation, where the transition to the unoccupied state is assumed to happen instantaneously, and the photoelectron does not interact with the rest of the system. Application of the sudden approximation allows one to write an equation for the photoemission intensity which distinctly defines the processes of electron removal and electron excitation as components of the equation which are themselves simple expressions. The photoemission intensity equation has the form: [12, 7, 6]

$$I(\mathbf{k}, \omega) = |M_{\mathbf{k}}|^2 f(\omega - \mu) \mathrm{Im} G(\mathbf{k}, \omega) \tag{10}$$

$\mathrm{Im} G$ is the imaginary portion of the spectral Green function describing the probability of adding or removing an electron with ($\mathbf{k}$, ω). The fermi distribution function $f(\omega - \mu)$ selects out for electron removal, and $|M_k|^2$ describes the probability of exciting the free electron to a higher energy state. Integrating this equation over the range of energies of a single band gives the equation for ARPES intensity spectra above. [28] Kaminski et.al. detail a method of extracting self-energy $\mathrm{Im}\Sigma(\omega)$ from this intensity spectra, which is used here. [14] The self-energy is in fact a sum of a real and an imaginary part; specifically the form is:

$$\Sigma(\omega) = \mathrm{Re}\Sigma(\omega) + i(\mathrm{Im}\Sigma(\omega)) \tag{11}$$

Group velocity is extracted from $\mathrm{Re}\Sigma(\omega)$, and electron lifetime is inversely related to $\mathrm{Im}\Sigma(\omega)$, which is related to the FWHM of EDC fit curves. [12]

The interaction probability $|M_k|^2$ arises from the interaction Hamiltonian M, which assumes homogeneity of the electron system to be valid in the Coulomb gauge. Multi-photon interaction with a single electron is also disregarded due

to its very low probability. Lastly, electron momentum is approximated to commute with a constant vector potential; the vector potential is constant in its independence of position due to the small interatomic spacing relative to incident photon wavelength. With these approximations, the interaction Hamiltonian takes on a simple form [7, 6]:

$$M = \frac{e}{m_e c} \overrightarrow{A} \cdot \overrightarrow{p} \tag{12}$$

Using this form of M_k in the expression for Intensity (Eq.10), we apply I($\mathbf{k}$,ω) to Energy and Momentum Distributed Curves fit to the ARPES spectra collected. Taking only the imaginary portion of I($\mathbf{k}$,ω) results in a Lorentzian form equation:

$$I(\overrightarrow{k} = k, \omega = \omega_0) = |M_{if}|^2 f(\omega_0) \frac{1}{\pi} \frac{\Sigma_{Im}(\omega_0)}{[\omega_0 - v_g k - \Sigma_{Re}(\omega_0)]^2 - [\Sigma_{Im}(\omega_0)]^2} \tag{13}$$

Applying features of a Lorentzian fit, $\text{Im}\Sigma(\omega)$ is the FWHM, with a peak centered at $\omega_0 = v_g k + \text{Re}\Sigma(\omega)$. MDC fits follow a simple Lorentzian form. EDC fits are based on Fermi Liquid Theory which add electron-electron interactions from quasiparticles and will follow, though not as well as MDC fits, the Lorentzian features in general. The FWHM of the Lorentzian fits give the quasiparticle scattering rate through the following relation [23]:

$$\Gamma(\omega) = 2 |\text{Im}\Sigma(\omega)| = (\text{FWHM}) * v_0(\omega) \tag{14}$$

From the rate of scattering we can examine the protected nature of surface states from specific types of interactions. MDC and EDC fits are discussed more thoroughly in Chapter 3.

2 History/Previous Work

The use of Bi_2Se_3 is predicated on its high quality relative to the other topological insulators which are in use so far, in ease of preparation and its relatively large bulk band energy gap of around 0.3 eV. Bi_2Se_3 also features simple surface states, which is preferable for the theoretical model behind the fit curves which are applied. A comparison of the current experimentally discovered TBI is shown in Figure 5 [1].

Type	Material	Band gap	Bulk transport	Remark
2D, $\nu = 1$	CdTe/HgTe/CdTe	< 10 meV	insulating	high mobility
2D, $\nu = 1$	AlSb/InAs/GaSb/AlSb	~4 meV	weakly insulating	gap is too small
3D (1;111)	$Bi_{1-x}Sb_x$	< 30 meV	weakly insulating	complex S.S.
3D (1;111)	Sb	semimetal	metallic	complex S.S.
3D (1;000)	Bi_2Se_3	0.3 eV	metallic	simple S.S.
3D (1;000)	Bi_2Te_3	0.17 eV	metallic	distorted S.S.
3D (1;000)	Sb_2Te_3	0.3 eV	metallic	heavily p-type
3D (1;000)	Bi_2Te_2Se	~0.2 eV	reasonably insulating	ρ_{xx} up to 6 Ωcm
3D (1;000)	$(Bi,Sb)_2Te_3$	< 0.2 eV	moderately insulating	mostly thin films
3D (1;000)	$Bi_{2-x}Sb_xTe_{3-y}Se_y$	< 0.3 eV	reasonably insulating	Dirac-cone engineering
3D (1;000)	$Bi_2Te_{1.6}S_{1.4}$	0.2 eV	metallic	n-type
3D (1;000)	$Bi_{1.1}Sb_{0.9}Te_2S$	0.2 eV	moderately insulating	ρ_{xx} up to 0.1 Ωcm
3D (1;000)	Sb_2Te_2Se	?	metallic	heavily p-type
3D (1;000)	$Bi_2(Te,Se)_2(Se,S)$	0.3 eV	semi-metallic	natural Kawazulite
3D (1;000)	$TlBiSe_2$	~0.35 eV	metallic	simple S.S., large gap
3D (1;000)	$TlBiTe_2$	~0.2 eV	metallic	distorted S.S.
3D (1;000)	$TlBi(S,Se)_2$	< 0.35 eV	metallic	topological P.T.
3D (1;000)	$PbBi_2Te_4$	~0.2 eV	metallic	S.S. nearly parabolic
3D (1;000)	$PbSb_2Te_4$	?	metallic	p-type
3D (1;000)	$GeBi_2Te_4$	0.18 eV	metallic	n-type
3D (1;000)	$PbBi_4Te_7$	0.2 eV	metallic	heavily n-type
3D (1;000)	$GeBi_{4-x}Sb_xTe_7$	0.1–0.2 eV	metallic	n (p) type at $x = 0$ (1)
3D (1;000)	$(PbSe)_5(Bi_2Se_3)_6$	0.5 eV	metallic	natural heterostructure
3D (1;000)	$(Bi_2)(Bi_2Se_{2.6}S_{0.4})$	semimetal	metallic	$(Bi_2)_n(Bi_2Se_3)_m$ series
3D (1;000)	$(Bi_2)(Bi_2Te_3)_2$	?	?	no data published yet
3D TCI	SnTe	0.3 eV (4.2 K)	metallic	Mirror TCI, $n_M = -2$
3D TCI	$Pb_{1-x}Sn_xTe$	< 0.3 eV	metallic	Mirror TCI, $n_M = -2$
3D TCI	$Pb_{0.77}Sn_{0.23}Se$	invert with T	metallic	Mirror TCI, $n_M = -2$
2D, $\nu = 1$?	Bi bilayer	~0.1 eV	?	not stable by itself
3D (1;000)?	Ag_2Te	?	metallic	famous for linear MR
3D (1;111)?	SmB_6	20 meV	insulating	possible Kondo TI
3D (0;001)?	$Bi_{14}Rh_3I_9$	0.27 eV	metallic	possible weak 3D TI
3D (1;000)?	$RBiPt$ (R = Lu, Dy, Gd)	zero gap	metallic	evidence negative
Weyl SM?	$Nd_2(Ir_{1-x}Rh_x)_2O_7$	zero gap	metallic	too preliminary

Figure 5: List of current TBI compiled by Yoichi Andos [1]. In the Remark column, SS = Surface States, PT = Phase Transition, and SM = Semi-Metal. The material used here, Bi2Se3, is highlighted.

2.1 History of TBI

The quantum spin hall effect, observed by Kato in 2004, depends on the presence of a large external applied magnetic field. The elimination of the necessity for a strong applied field was proposed later in 2004 by Murakami, Nagaosa, and Zhang. [22] A model proposed by Kane and Mele [15] to observe QSH effect through spin-orbit coupling in graphene was experimentally difficult to observe due to the weakness of the interaction. Finally in 2007, Konig et. al. [17] confirmed observation of the QSH in heavy metal quantum wells CdTe and HgTe as proposed by Bernevig, Hughes, and Zhang [3]. Moore and Balent in 2007 [21] followed this with a model predicting the observation of 3D systems which could display quantum spin hall effects, and proposed the term topological insulator to describe this class of materials.

Topological insulators are a material which are insulating in the bulk and conductive on its surface. It differs from a normal insulator coated with a conductor because the conducting surface states of a topological insulator arise from bulk properties rather than surface conditions. Bloch wavefunctions of the bulk states define a topological number Z_2, which defines a material as a strong or weak topological insulator. For a strong topological insulator (Z_2 = 1), the bulk has a bulk gap while surface states remain gapless. The characteristics of the surface states only change when the bulk gap is closed by changes to the system parameters; consequently, surface conductivity is robust against ordinarily significant effects such as nonmagnetic impurities and elastic backscattering at the edge. For a 3D topological insulator, 3 other topological numbers (v_1, v_2, v_3) define the dispersion and shape of the Fermi surface. Bi_2Se_3 has a Dirac cone dispersion, which is similar to that of graphene and has a linear (massless electron) form near the Dirac point. [22]

Another significant characteristic of topological insulators, in addition to its

robustness against disorder in normal temperature and magnetic field levels, is the spin-locked behavior of conducting electrons at the surface states. The spin and the direction of motion of the conducting electrons are locked, such that they create a coherently spin current; the strength of this effect is 2-3 orders of magnitude stronger than when observed in an ordinary quantum well. [20] The work presented here is based on papers by Park et. al. 2010 [24] and Pan et. al. 2012 [23] , both of which addressed quasiparticle interactions observed in TBI through MDC analysis. EDC analysis was also done to define the boundary of the bulk conduction band.

2.2 Quasi-particle Scattering

Based on previous work which verified the existence of spin chiral states in the topological metallic regions of Bi_2Se_3, Park et. al. [24] presented evidence of the protected nature of these states: ARPES data showed sharp peaks in the data caused by long lifetimes of the quasi-particles in the protected state. The robustness of the protected topological states were also tested by taking data four days after cleaving the test surface to allow for surface effects to affect the experimental surface. The data showing the spread of energy of the aged surface in comparison to the freshly cleaved surface is shown in Figure 7.

A long quasiparticle lifetime, an indicator of protected topological metallic states, is a critical characteristic of useful material application. Because long lifetime corresponds to a small value of imaginary self-energy, protected states manifest in ARPES data as sharp line shapes. Equally interesting to the applicability of topological metallic materials is the methods of scattering which affect the quasiparticle scattering. Park et.al. analyzed the scattering of conduction electrons in the topological band of Bi_2Se_3 into bulk states; the analysis showed that the surface states were robust against surface adsorbate impurity
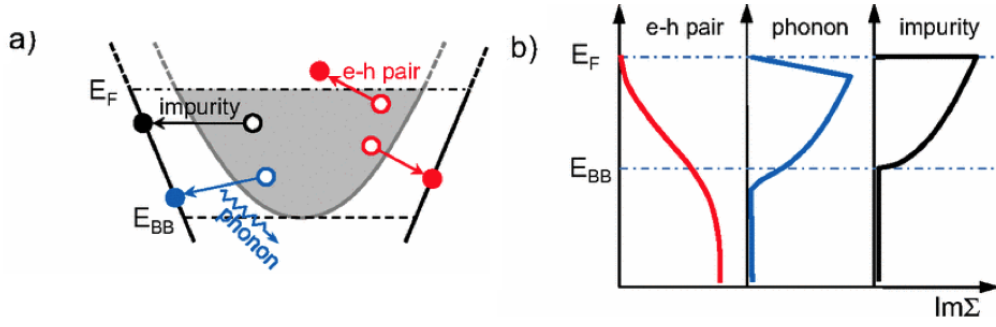
Figure 6: (a). Scattering methods in the topological metallic band.[24] A hole in the topological band can create an electron-hole pair, emit or absorb a phonon, or decay into a bulk electronic state through interaction with an impurity potential. (b). $\text{Im}\Sigma$, inversely proportional to quasi-particle lifetime, for the different scattering methods. States which have binding energies lower than the bulk band bottom scatter mainly through phonon- or impurity-interaction channels. However for binding energies that are higher than the bulk band bottom, the main scattering channel becomes electron-hole pair production.

scattering, as described in Figure 6b.

ARPES energy-momentum distribution data taken on a sample of Bi_2Se_3 after aging the surface 4 days shows the dirac point shifts to a higher binding energy compared to data taken on a fresh surface. The magnitude of the difference measured by Park et.al. was about 0.1 eV, and likely arises from the disturbance of the electronic structure from the adsorbed molecules contributing a charge to the aged surface.

Data was also taken on the 4 day aged surface with a higher range of photon energies. As photon energy increases, the lifetime of the resulting photoelectron decreases; the bulk conduction band's lower boundary edge becomes clearly defined at the higher photon energies where it remained indistinguishable at the lower (8 eV) value. Overall, a uniform shift of about 0.1 eV of the band edges can be observed in the fresh v.s. aged surfaces: the dirac point shifts from 0.33 to 0.43 eV, while the bulk conduction band lower boundary goes from 0.1 to 0.2 eV.

There are three main methods of scattering from the topological band states to states in the bulk (conduction) band. States with binding energies which are lower than the bulk conduction bands lower edge (here, 0.2 eV) scatter through phonon emission/absorption or impurity induced charge potentials. However, for states with energies higher than the bulk conduction bands bottom edge, the main channel open for scattering and decay is through electron-hole pair production, which conserves the total energy and momentum.

ARPES data is particularly efficient for extracting the self-energy ImΣ of the topological electrons. The momentum-energy spectral intensity collected through ARPES is proportional to the imaginary part of the Green function ImG, which can be put in terms of ImΣ, or the electron self-energy, which is in turn inversely proportional to the particle lifetime:

$$\text{Im } G(k,\omega) = \frac{Im\Sigma(k,\omega)}{[\omega - \epsilon_k - Re\Sigma(k,\omega)]^2 + Im\Sigma(k,\omega)^2}$$

For correlated systems, the lifetime is considered through the quasiparticle scattering rate $\Gamma(\omega)$:

$$\Gamma(\omega) = 2\left|\text{Im}\Sigma(\omega)\right|$$

The electron self energy ImΣ, in turn, can be calculated from Lorentzian fits on the momentum distribution curves (MDCs) of the ARPES spectra:

$$2|\text{Im}\Sigma(\omega)| = \Delta k(\omega)v_0(\omega)$$

where Δk is the full width-half maximum (FWHM) of the MDC lorentzian peak, and v_0 is the group velocity. [23] Lastly, the calculations are done for the ARPES spectra taken at the photon energy which most suppresses the bulk band contribution to the spectral function. Due to k_z selection rules, photoelectrons from the bulk do not show up as strongly at this lower energy, and allows more selective analysis of the topological metallic bands.
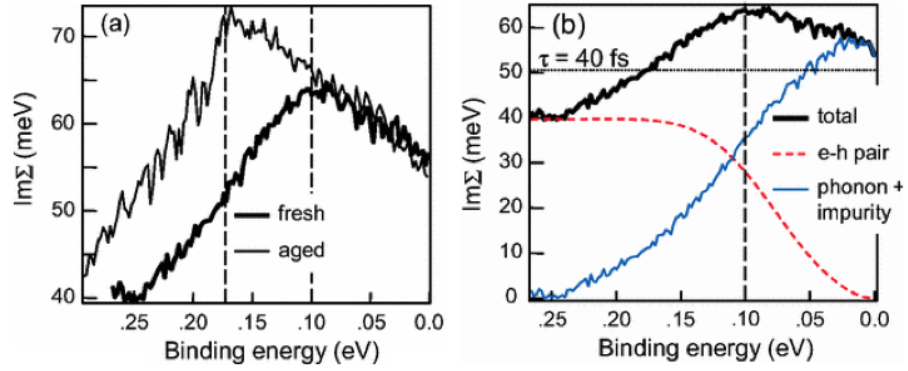
Figure 7: Plot of the ImΣ as a function of decreasing binding energy, for both fresh and aged samples. For both the fresh and the aged samples, ImΣ decreases above the bulk conduction band bottom. This is indication that the main method of scattering is through states which do not exist beyond the bulk conduction band. Since the bulk conduction bottom edge is the approximate point at which electron-hole pair creation (electron-electron interaction) channels, and the phonon and impurity scattering channels, exchange dominance levels in contributing to ImΣ in (b)., and the lack of an observable kink indicating phonon scattering, Park et.al. conclude that the dominant channel within the low energy, bulk conduction band range is through impurity scattering. [24]

At an approximation of one electron per unit cell at the Fermi surface, and one donated electron per adsorbate atom on an aged surface, with ideal localization of the donated electrons to surface states, an interadsorbate distance of less than 13Å is calculated by Park et.al. from the observed 2.3% increase in Fermi surface volume of the aged (v.s. fresh) samples. The increase of adsorbates in an aged sample increases the surface disorder potential, which would decrease the quasiparticle lifetime (i.e. increase the value of ImΣ) at low binding energies near E_F. However, Fig.7a shows no such behavior near E_F.

The best case explanation for the lack of observed effect from the adsorbates on surface state electron self-energy would be that the topological metallic states are protected from small surface potential disorders. This is the conclusion that Park et.al. tentatively suggest with their work on extracting ImΣ of Bi_2Se_3 from MDC and EDCs of ARPES spectra. However, they caution that it has been shown in a similar, quasiparticle metal-insulator transition state (Bostwick et.al. 2009 [4]), that the type of adsorbate will have varying degrees of influence on the induced surface potential, and that this must be resolved before a conclusion on the protected nature of topological states from small induced potentials can be made.

2.3 Weak surface electron-phonon interaction: the coupling constant

The calculation of the electron-phonon coupling constant λ from the ARPES intensity spectrum can be used to determine if the topological metallic states are protected.

We refer back to the expressions for scattering rate $\Gamma(\omega)$, self-energy Im$\Sigma(\omega)$, and Lorentzian peak width Δk from the previous section,

$$\Gamma(\omega) = 2\left|\text{Im}\Sigma(\omega)\right|$$

and

$$2|\text{Im}\Sigma(\omega)| = \Delta k(\omega)v_0(\omega).$$

MDCs can be done on a section of the ARPES spectra that is not affected by the bulk valence band (above the dirac point); Pan et.al., in Fig. 8, shows the $\text{Im}\Sigma$ and Δk for data taken at 18 K, which has its Dirac point at 0.27 eV. The Lorentzian fits here are good as the MDCs above 0.27 eV show two clear peaks without convolution with a bulk background. Due to the energy dependence of v_0, $\text{Im}\Sigma$ has a less obvious energy dependence overall compared to Δk; however, both show little change between spectra at 18 K and 255 K as they approach the Fermi energy. This lack of temperature dependence near the surface suggests little to no increase of phonon scattering, which would increase with temperature, and has a very weak phonon-surface state coupling constant, in agreement with Park et.al [24].

The coupling constant λ is calculated by the approximately linear expression for $\text{Im}\Sigma(\omega)$ at a higher temperature regime ($k_B T > \frac{\Omega_0}{3}$, where Ω_0 is the maximum phonon energy) [16]:

$$\text{Im}\Sigma(\omega) = \lambda \pi_B T$$

Pan et.al. plot $\text{Im}\Sigma$ v.s. temperature from low T to room temperature for three samples each at low (18.7 eV) and high (50 eV) photon energy. The data at each temperature was averaged over a range of ω (-20 meV $< \omega <$0). Though the magnitudes of $\text{Im}\Sigma$ varied due to instrumental and environmental variational effects, the rate of change with respect to temperature all displayed similar upward slopes. They present a linear fit value for λ to be very weak: one sample at $\lambda_1 = 0.076 \pm 0.007$ and a second at $\lambda_2 = 0.088 \pm 0.009$. The weak phonon coupling agrees with expected lack of temperature dependence
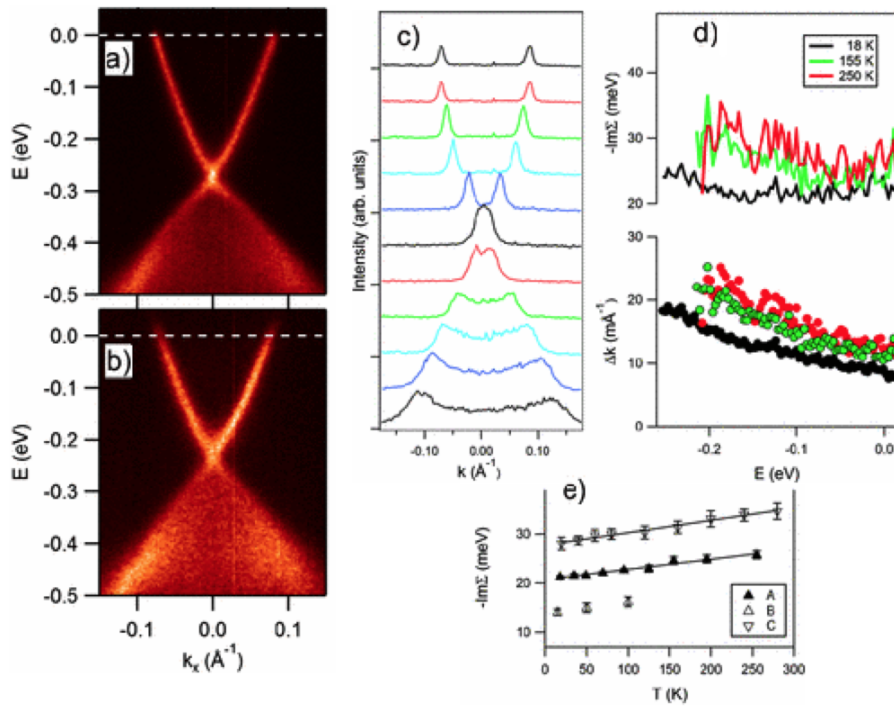
Figure 8: Spectra, MDC, and calculation of λ by Pan et.al. 2012. ARPES spectra at 18 K (a) and 255 K (b) show the upward shift of the Dirac point from $\sim$0.23 eV to $\sim$0.27 eV. (c). Selected MDC fits done on the 255 K spectra. (d). ImΣ and Δ k at temperatures from 18 K to 250 K. There is a lack of temperature broadening observed near E_K. (e). ImΣ as a function of T, from which Pan et.al. derives their value of λ. [24]

within the surface states. Other studies have shown [1, 3, 22] that bulk states have a much stronger coupling to the surface; one calculation by W. McMillan [19], predicts $\lambda = 0.6$ for Bi_2Se_3. Pan et.al. note that due to experimental constraints at lower temperatures, their calculated value of λ above could be undervalued. In general, both works by Park 2010 and Pan 2012 conclude that metallic surface states on topological insulators (Bi_2Te_3 and Bi_2Se_3) display weak electron-phonon coupling and are topologically protected from low-energy impurity scattering.

3 Data and Analysis

3.1 Lineshape analysis for ARPES

There are two modes of lineshape analysis used for the momentum-energy maps gathered through ARPES in this work. The two modes use different fit models, since energy distributions are more significantly affected by many-body interactions than momentum distributions due to effects from transport through the surface. Because of this, the EDC (energy distribution curve) analysis includes Fermi Liquid Theory in its fit curves, while the MDC (momentum distribution curve) models are purely Lorentzian-based.

The incident photon energies and temperatures were varied to find the clearest spectra which minimizes the bulk conduction band visible below the Fermi energy. Spectra taken at 11 eV were seen to have minimal BCB inclusion. There is also an approximately linear temperature dependence observed for the Dirac point binding energy: as temperature decreases, the DP binding energy increases at a rate of around 50 meV per 100 K decrease.

Data and analysis in this work is based off the quasiparticle EDC and MDC work done by Park 2010 and Pan 2012 discussed in the previous chapter.

The topological insulator parent compound Bi_2Se_3, with a comparatively low measured Dirac point self energy of 150 meV, was chosen for analysis. The single crystals (2mm x 2mm x 0.05mm) were grown by the group of Dr. Genda Gu at Brookhaven National Laboratory [25] by a self-flux method in a 97% Se / 3% Bi solution. The high purity raw material was sealed in a quartz tube and raised to 700°C for 12 hours, then rocked for 2 hours at that temperature. The solution at one end was cooled to 455°C at a rate of 0.5°C per hour and kept for 2 hours at that temperature. The solution was then transferred to the other end of the quartz tube and cooled to room temperature at a rate of 10°C per hour.
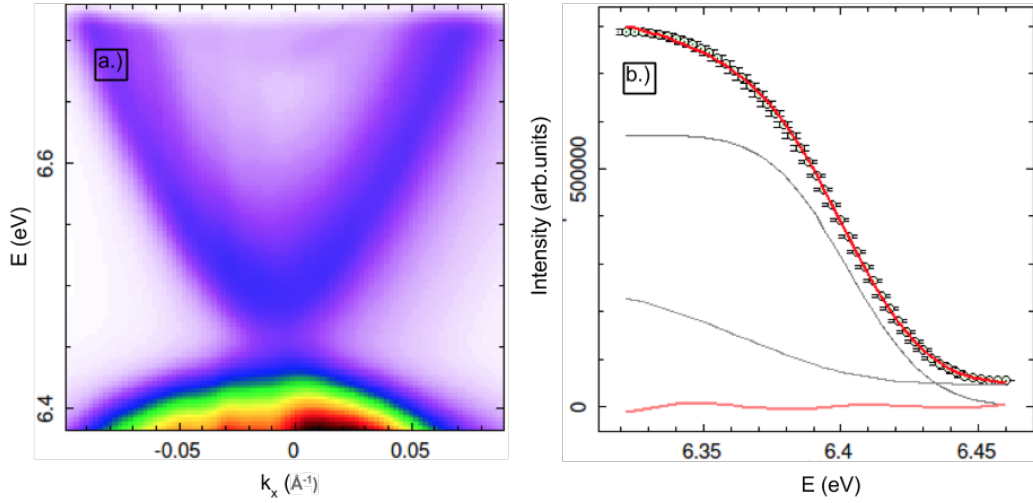

Figure 9: Fermi edge fit done at 25 K spectra. (a) Intensity spectra at 25 K. (b) The Fermi Dirac distribution fit to the energy distribution at k = 0.

The crystals were cleaved in-situ in ultra high vacuum ($\sim$5x10^{-11} Torr) at beamline 5-4 at the Stanford Synchrotron Radiation Lightsource (SSRL) at SLAC in Menlo Park, CA. From an available range of photon energies from 7.5 eV to 25 eV, a photon energy of 11 eV produced the cleanest data with maximal suppression of the bulk states. The energy and angle resolution is 15 meV and 0.3°, respectively.
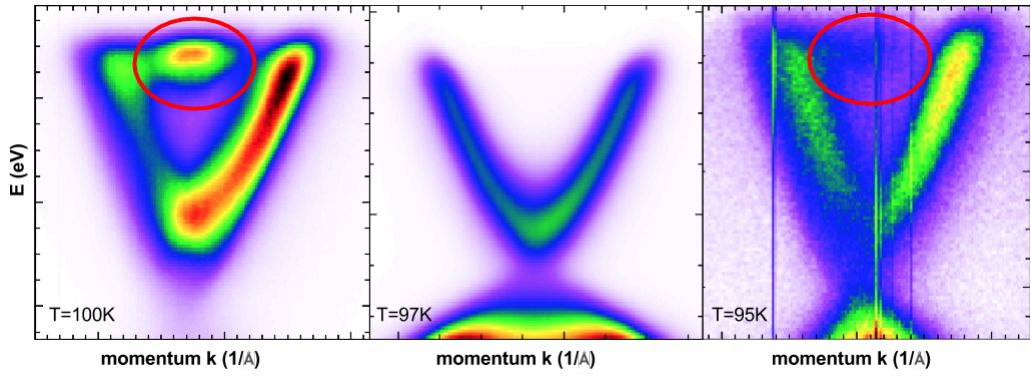
Figure 10: ARPES spectra at different photon energies, at ~100K. Bulk conduction band is visible in the 7.5 eV and 25 eV spectra, circled in red. The BCB is suppressed at 11 eV.

The cleanest data was selected from three different sample runs, and is presented in this chapter. Spectra was taken for temperature dependence from 50 K to 300 K in steps of 25 K, with Lorentzian Fermi Liquid Theory (FLS) fits applied to Energy Distribution Curves (EDCs) and Lorentzian fits applied to Momentum Distribution Curves (MDCs) performed on the collected spectral data.
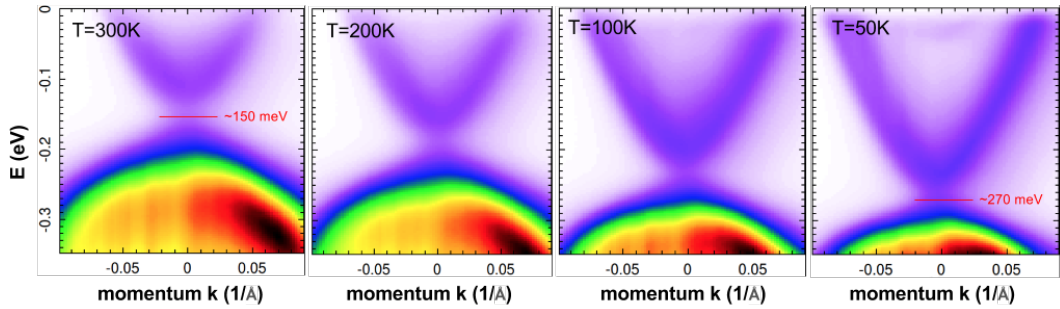

Figure 11: Temperature dependence of Dirac point energy. A decrease of 100 K corresponds to an approximate 50 meV increase in the Dirac point binding energy.

Temperature dependence of the spectra can be compared to the samples used by Pan 2012 and Park 2010. As seen in Fig.11, the Dirac point energy in-

creases $\sim$120 meV for a temperature change from 300 K down to 50 K. The broadening of the surface states due to electron-electron and electron-phonon coupling also indicates a decrease in quasiparticle lifetime; note that the effect on lifetime from impurity scattering is not a significant component, as there is little dependence observed from proximity to the fermi edge. The comparatively low Dirac point energy, around $\sim$150 meV at 300 K, indicates a high quality sample, with lower quasiparticle interactions than the samples used by Pan 2012 and Park 2010 which display a larger band gap.

3.2 Quasi-particle Interaction Observations

When optimizing the EDC fits on initial data, an additional Gaussian convolution improved the fits over a simple Lorentzian based Fermi Liquid Theory model. In Figure 12a, the magnitude of the convolution was measured through its FWHM for the spread of momentum, at various temperature values from 300 K to 149 K. The convolution decreases with lower temperature and momentum, which indicates the source of the convolution is from electron-phonon interactions.

An example of broad, non-ideal data is shown in Fig.12b. The Lorentzian FLS fits, in dotted circles, are done along EDCs indicated directionally by the red line. Near the Fermi edge, where quasiparticle electron-phonon interactions are strongest, the fits were improved with the additional Gaussian convolution, which is plotted for T= 149, 190, 275, 287, 294, 298, and 300 K in Fig.12a. Subsequent data was optimized for sharp spectra along the energy axis to reduce the convolution contribution.
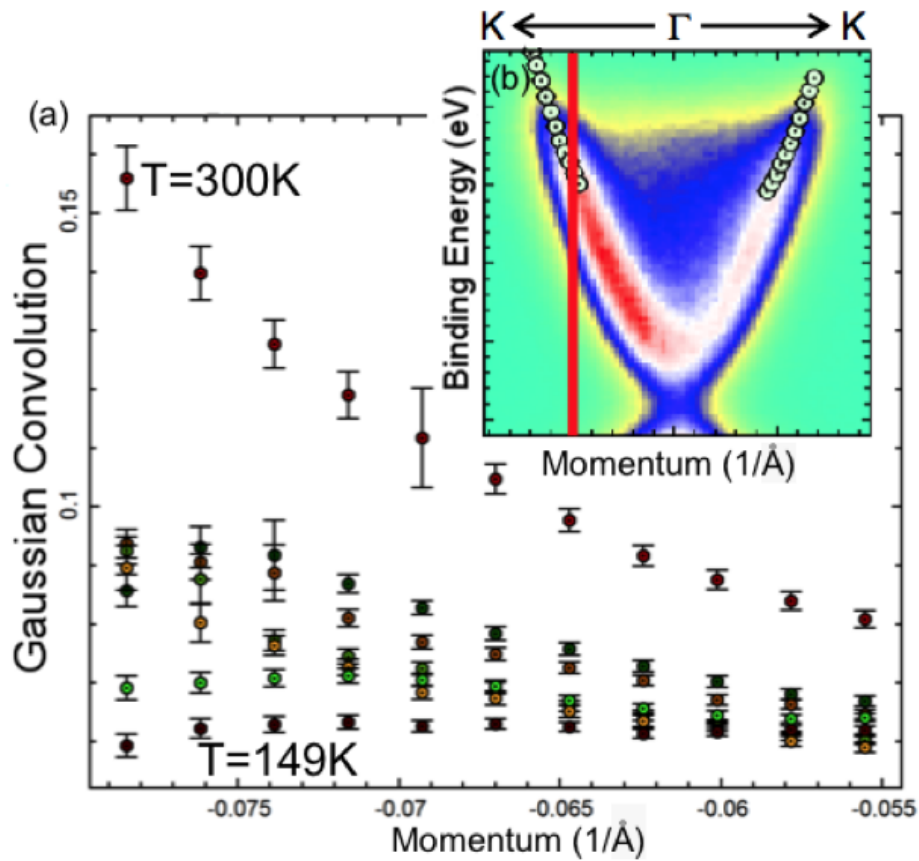
Figure 12: (a). The Gaussian convolution ($\sim$FWHM) as a function of momentum. The convolution is measured at several temperatures between 149 K and 300 K. (b). An example of an EDC slice along select value of momentum. The FWHM of the EDC peak is taken as a measure of the Gaussian convolution at that momentum. Figure from Reichwein, [25].

3.3 EDC line shape analysis

The broadening observed in the spectra arises from many-body effects. Temperature also affects the spread observed in the EDC fits. Minimizing the spread reduces the need for adjustments to the fit model to accommodate these effects. In this work, the fits are modeled by the Fermi Liquid Theory, which introduces three parameters: ω_0, Z, and η– respectively, they determine the ARPES kink location, scale the dispersion $\epsilon(k)$ relating to the spectral function A(k,ω), and specify the quasiparticle lifetime.

The fit function applied to the momentum-energy dispersion has the form:

$$\epsilon(k) = v_f(\sqrt{|k - \delta k|^2 + \Delta_v^2} - \Delta E) \tag{15}$$

where v_f is the Fermi velocity, δk is the difference of the Dirac-point momentum from the gamma-point Γ, Δ is the size of the gap at the Dirac point, $\Delta_v = \frac{\Delta}{v_f} << 1$, and ΔE is the shift applied to the experimental Fermi crossing point. Note that as k approaches either 0 or a large limit, the dispersion relation becomes parabolic or linear, respectively.

Plotting the peaks of EDC fits to the ARPES spectra, the peaks should follow the dispersion above, with approximately linear form near the Fermi edge and parabolic around the Dirac point.

Figure 13 shows the dispersion and EDC fits done at several different temperatures. EDC fits are shown to become poorer at high temperatures, when many-body effects become stronger.

The parameter values of Eq.15, aside from the fermi velocity v_f, were determined and set at those fit for 50 K. The Fermi velocity decreased with increasing temperature. Both EDC and MDC comparisons yielded matching results for v_f.

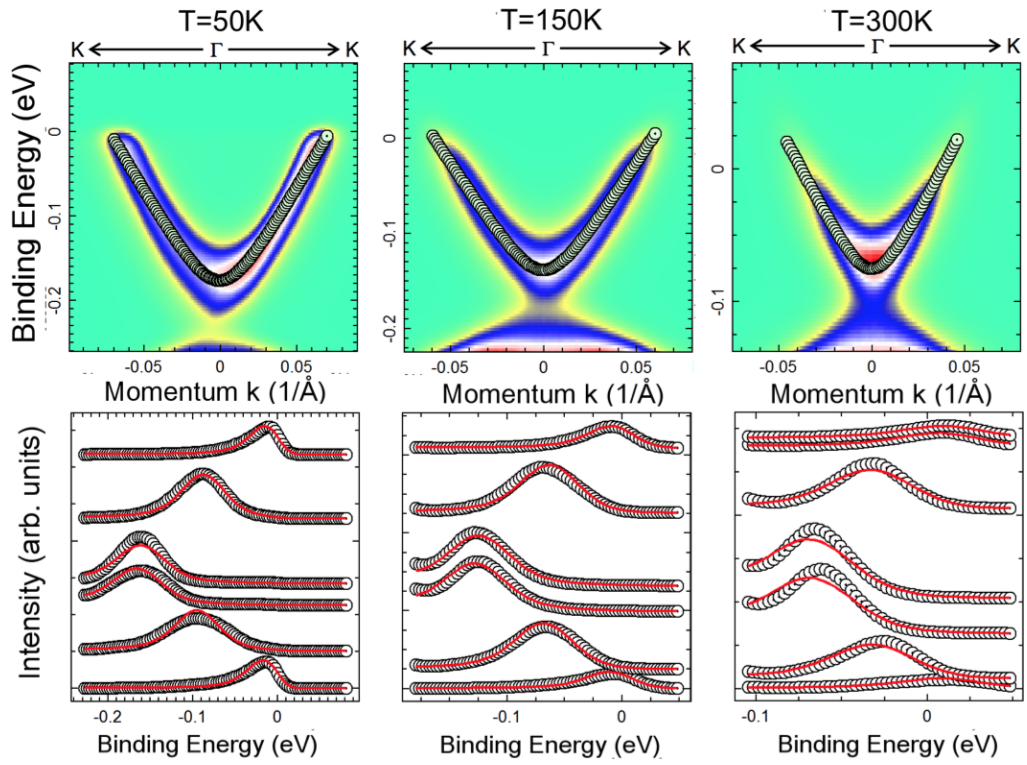The EDC fits were then done again onto smaller constrained regions of the

Figure 13: EDC and dispersion fits are shown on ARPES spectra for 50 K, 150 K, and 300 K. The dispersion Eq.15 is applied to the EDC peaks in the top row. Lorentzian FLS EDC fits are shown for select values of momentum in the bottom row. Figure from Reichwein, [25].

ARPES spectra dispersion, using the same FLS parameter values used in Figure 13. Values were set at Z = 0.8, $\omega_0 = 0.99$ and $\eta = 0.015$, with varied non-zero values for the convolution, baseline, and spectral weight. Regions were cut to include the left and right linear dispersion near the Fermi edge, and the approximately parabolic region around the Dirac point with higher electron self-energy. The EDC fits for these regions are shown in Figure 14.
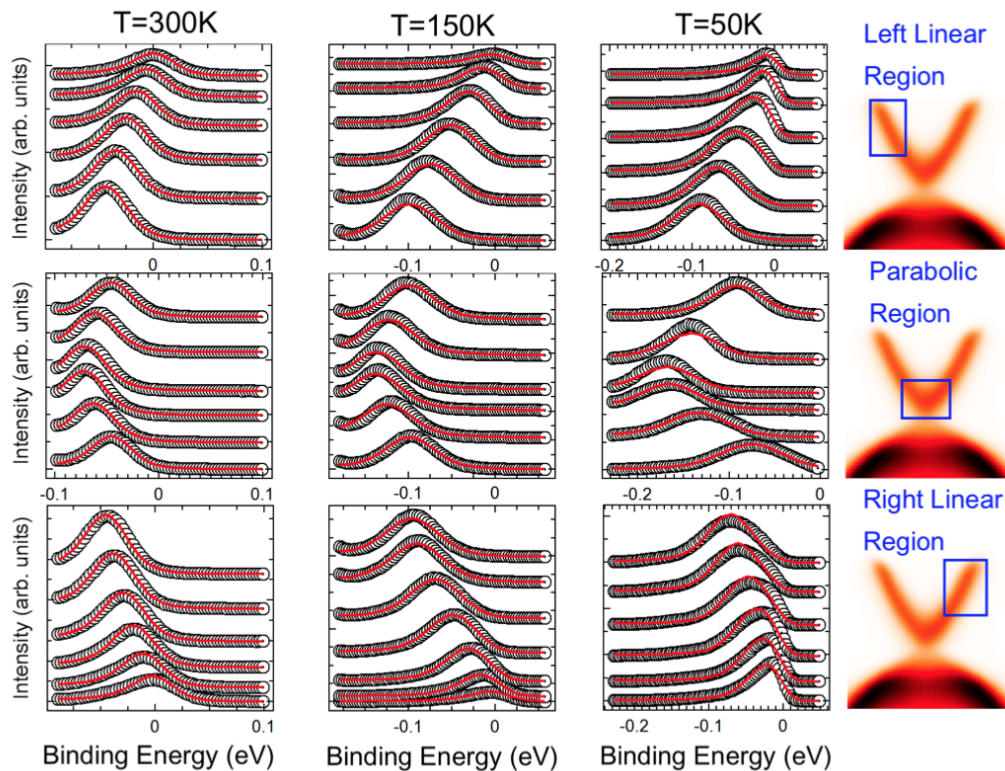

Figure 14: FLS EDC fits on constrained linear and parabolic regions of the ARPES spectra. The parameters of the dispersion equation 15 were kept from the fits done in Figure 13. Spectra was fit at several temperatures, 50 K, 150 K, and 300 K. The poor fits in the parabolic region compared the linear left and right regions is apparent.

Though the dispersion equation 15 has a parabolic form at the low momentum/high binding energy region near the Dirac point, the experimental spectra shows the area is not perfectly parabolic. This is due to electron-phonon coupling in this region which is not accounted for fully in the FLS model which the

dispersion relation is based on. Away from high binding energy regions, MDC and EDC FLS models display good general agreement for electron self-energy calculations.

3.4 MDC line shape analysis

The ARPES spectra was analyzed with MDC fits to compare to the Gaussian-convoluted EDC analysis done in the previous section. MDC fits are modeled on a simple Lorentzian theory; compared to EDCs with a simple Lorentzian base (i.e. no FLS or Gaussian convolution included), MDC fits produce excellent fits aside from a slight observable asymmetry around the Dirac point. The asymmetry is ascribed to the change in the momentums lattice direction depending on its sign; this is a negligible effect in self-energy analysis. Therefore, the full width half maximum (FWHM) was constrained to be equal for both peaks around the Dirac point when extracting fits from the MDC analysis. From before, we have the relation:

$$2|\text{Im}\Sigma(\omega)| = \Delta k(\omega)v_0(\omega)$$

Where Δk is the FWHM of the MDC fits. The imaginary complex self energy can be extracted from the fit and group velocity v_0. Figure 15 presents the MDC fits at several temperatures.

The peak locations of the MDC fits are in good agreement, although some unevenness arises in intensity due to differences in crystallographic direction when taking data along positive or negative momenta values; this has a negligible effect on the analysis.

3.5 A comparison of MDC and EDC analysis

A comparison of the imaginary self-energy of the MDC and EDC analysis yields information about which interactions are dominant in Bi_2Se_3. The MDC self-
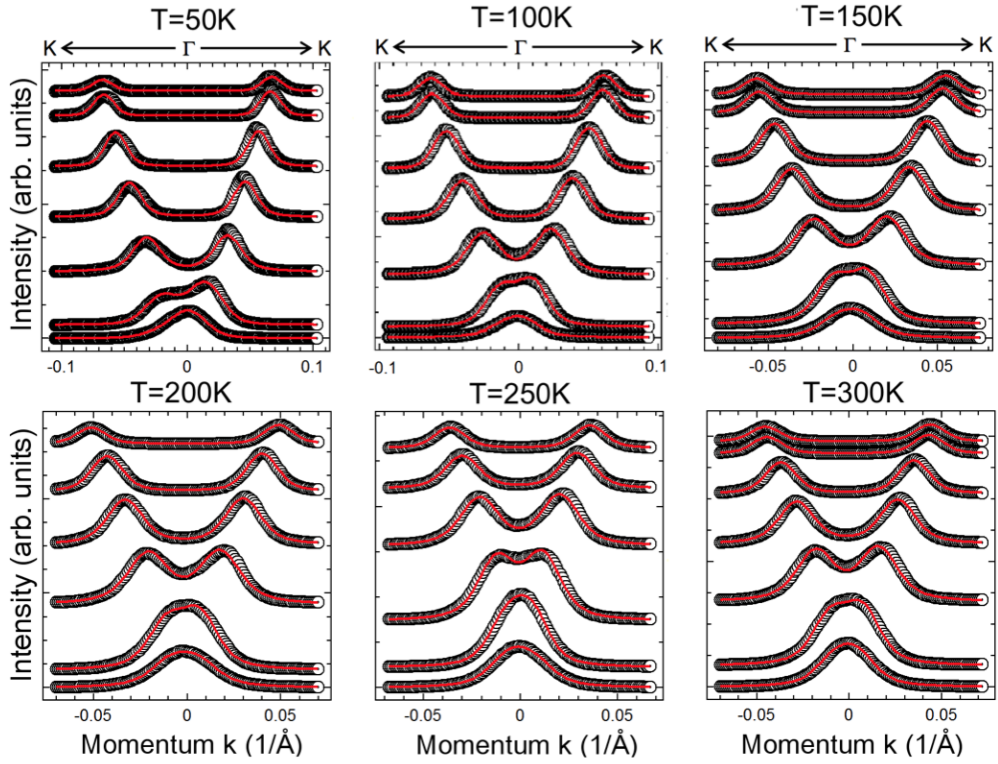
Figure 15: MDC fits on ARPES spectra at various temperatures. The asymmetry of the peak pairs is due to changing lattice direction along negative and positive momenta. FWHM for each peak pair was constrained to be equal when used to extract $\text{Im}\Sigma(\omega)$.

energy from ImΣ were compared against the theoretical values predicted by FLS theory, which were calculated using the parameters determined through the EDC fits done in the previous section. A spike in ImΣ near the Fermi edge would indicate lattice interactions and impurity scattering, resulting in shorter quasiparticle lifetime, i.e. higher ImΣ. This can be attributed to the increase in scattering to the bulk band from surface impurities. Alternatively, electron-hole pair production dominates within the high energy range, as discussed in section 2.

From our MDC and EDC fits done above, the imaginary self energy ImΣ was extracted and is plotted in Figure 16. A comparison between the data extracted from MDC fits and the values calculated for the FLS EDC fits (using the same parameters determined in section 3.2) at various temperatures from 50 K to 300 K is done below.
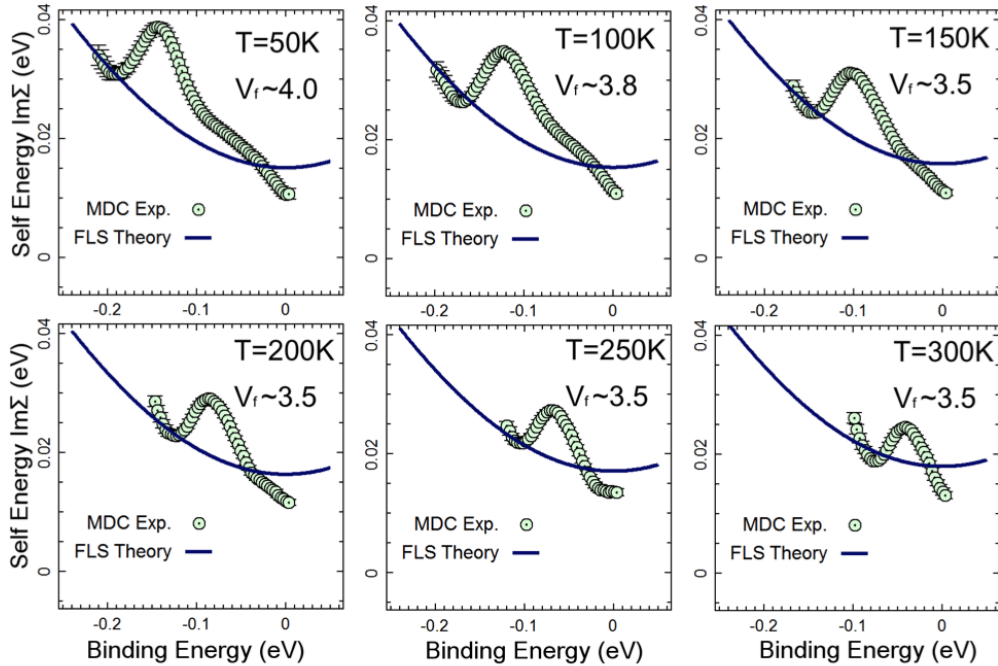

Figure 16: Extracted ImΣ from FLS EDCs (black line) and Lorentzian-based MDCs (circles). The BCB extends down to around 50 meV, dependent on temperature. No spike in ImΣ is seen near the Fermi edge.

33

The absence of a peak in self-energy near the Fermi surface (set at 0 eV binding energy) is apparent in Figure 16. Surface impurity and phonon interaction scattering from surface to bulk states would be expected to dominate at these lower energies. However, no such peak is seen. This could be indication that the surface states are protected from smaller impurity scattering. On the contrary, electron-electron interaction does increase with increasing binding energy as expected, as indicated by the concurrent increase of $Im\Sigma$ with increasing energy.

There is a spike seen in the Lorentzian-MDC fits in the higher binding energy range. This spike would be expected to be seen in the low-energy region to indicate electron-phonon scattering. However, the BCB is seen to extend only to around 50 meV. The location of the spike well below the bulk range suggest these are intra-surface interactions. The magnitude of the spike in self-energy is relatively large. Electron-phonon scattering results in a large change in momentum, but a small change in energy. The magnitude of each phonon excitation is much smaller than the spike observed in the self-energy shown in Figure 16. We suggest this is explained by many small-magnitude phonon interactions occurring between surface states.

Although there is no large spike within the range of the bulk conduction band (E_F to 50 meV), there is an observable change in the slope which occurs, for example, at around 30 meV for the fits done for 250 K. This kink in the slope is, as stated previously, indicative of electron-phonon interactions, and does occur in the low energy range. So while there is indeed evidence for electron-phonon interaction from the surface to the bulk states, the location of the large peak well below the bulk suggests intra-surface and surface-impurity scattering is strongest in higher energy ranges.

Lastly, we explain the discrepancy between the EDC and MDC fits in Figure Fig.3.7. The main effect, which has been discussed previously, is that the

FLS model on which the EDC fits are based only incorporate electron-electron interactions. The electron-phonon and impurity scattering has non-negligible effect on the dispersion. Unfortunately, incorporating these effects into theory is difficult to implement in its complexity. The other point to note is the inconsistent dependence of v_f on temperature. The dispersion relation $\epsilon(k)$ shifts its parabolic dispersion upward with increasing temperature. Since v_f remains at the Fermi edge, this decreases the slope of the dispersion at the edge and hence the magnitude of v_f. An increase of temperature should proportionally decrease the Fermi velocity v_f. However, the inconsistency appears when the change in v_f levels off rather than continuing to decrease as expected. The discrepancy was addressed here by adjusting the constraint function used in the dispersion relation equation at each temperature, although the fit parameters were kept consistent.

3.6 Initial Weak Electron-Phonon Coupling in Surface States

By taking the expression for the imaginary part of self-energy (ImΣ) at the high temperature limit $k_B T < \frac{\Omega_0}{3}$, we get to a linear form:

$$\text{Im}\Sigma = \lambda\pi k_B T$$

where λ is the electron-phonon coupling constant. Giraud and Egger [10] published a theoretical value for λ_{k_F} of strong TI (Bi_2Te_3) to be around λ_{k_F} = 0.13. However, Pan et.al. [23] measures a value of either $\lambda = 0.076 \pm 0.007$ or $\lambda = 0.088 \pm 0.009$ on different crystal samples of Bi_2Se_3, an order of magnitude lower; they attribute this to the absence of temperature-broadening. In addition, the values are in contrast to values obtained for Cu-doped samples of Bi_2Se_3, which are on the same order as reported by Giraud and Egger.
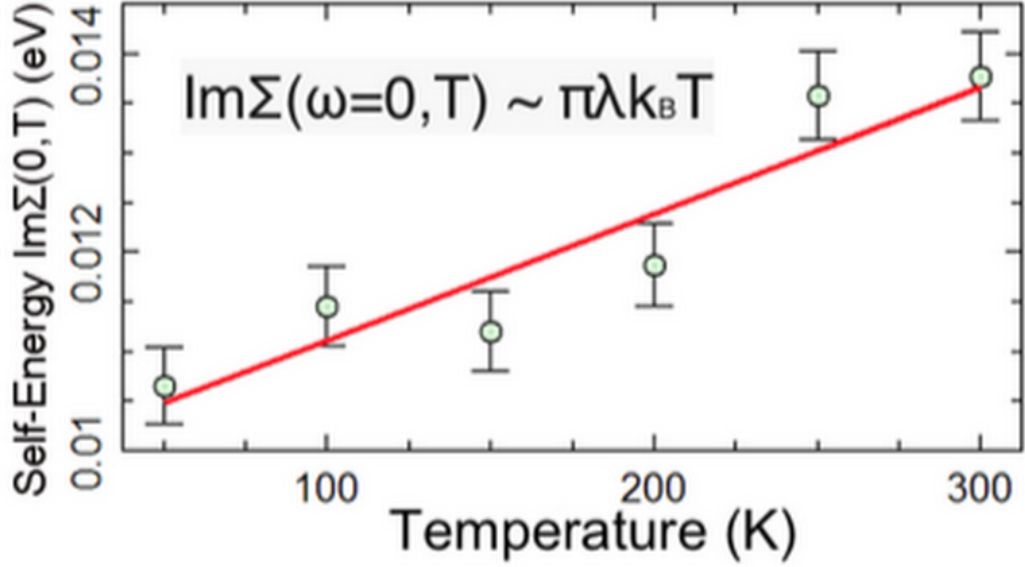
Figure 17: Plot of ImΣ against temperature at $\omega = 0$. Slope is used to extract the electron-phonon coupling constant λ. [25]

The plot of our data for ImΣ as a function of temperature, at the gamma point $\omega = 0$, yielded similar results to Pan et. al, and is plotted in Figure 17. Initial results yield, for Bi_2Se_3, a coupling constant $\lambda = 0.049 \pm 0.007$. This value, obtained by Eric Reichwein using the set of data collected on the ARPES run date used for the previously discussed analysis, is the lowest coupling constant yet measured, around 35% lower than the value of 0.076 obtained by Pan on the same material.

3.7 Further Determination of the Coupling Constant

The coupling constant was determined, on an earlier collection run of temperature-dependence data taken on the same crystal sample of Bi_2Se_3. The sample was freshly cleaved at the same beamline and ARPES data was collected with the same method mentioned above. The constant was calculated using a linear fit to both the entire fit data set, and again with the fit restricted to lower E, excluding the MDC fits that begin to exhibit a change in behavior at higher

energy near the Dirac point.

The MDC's were done on two different cuts of the momentum-energy intensity spectra. MDC fits exhibit a change in behavior going between the linear *leftorright* and the parabolic center regions, at lower and higher energy levels respectively. There is a kink in the behavior of the curves at the transition, which makes a continuous fit to the position of the MDC peaks, for example, very poor. An analysis of the entire ćontinuoużregion of the right side was done for the purpose of observing how the coupling constant would be affected.

The entire continuous right side regional fit is shown in Figure 18. The break observed in the peak position data points at E = -0.130 eV makes the beginning of a much steeper slope region than compared to the fit slope of the region between E = -0.130 eV and E = 0 eV. Fitting to the entire region results in a slope that is flatter than for the linear low energy region alone. Consequently, the extracted Fermi velocity is also determined to be lower.

When only the linear, low-energy region of the spectra is analyzed as shown in Figure 19, the linear fit to the MDC peak positions displays much lower error due to the lack of effect from the changed behavior at the higher energy parabolic region around k = 0. As demonstrated by the fit comparison in Figure 19, a properly restricted analysis distinguishing between linear and parabolic regions will have a steeper slope, and a higher Fermi velocity.

The unrestricted, including both linear and parabolic regions, analysis of the coupling constant is shown now, before the results for the more properly restricted, linear-region-only analysis:

In comparison, the value of lambda obtained from the low-E linear-only region fits is much lower, by a factor of two:

The value obtained for this second data set run, on the same sample as in the previous section, is shown in Figure 21. Lambda is calculated to be $\lambda = 0.078$, which is higher than Reichwein's determination of $\lambda = 0.049$, but within error
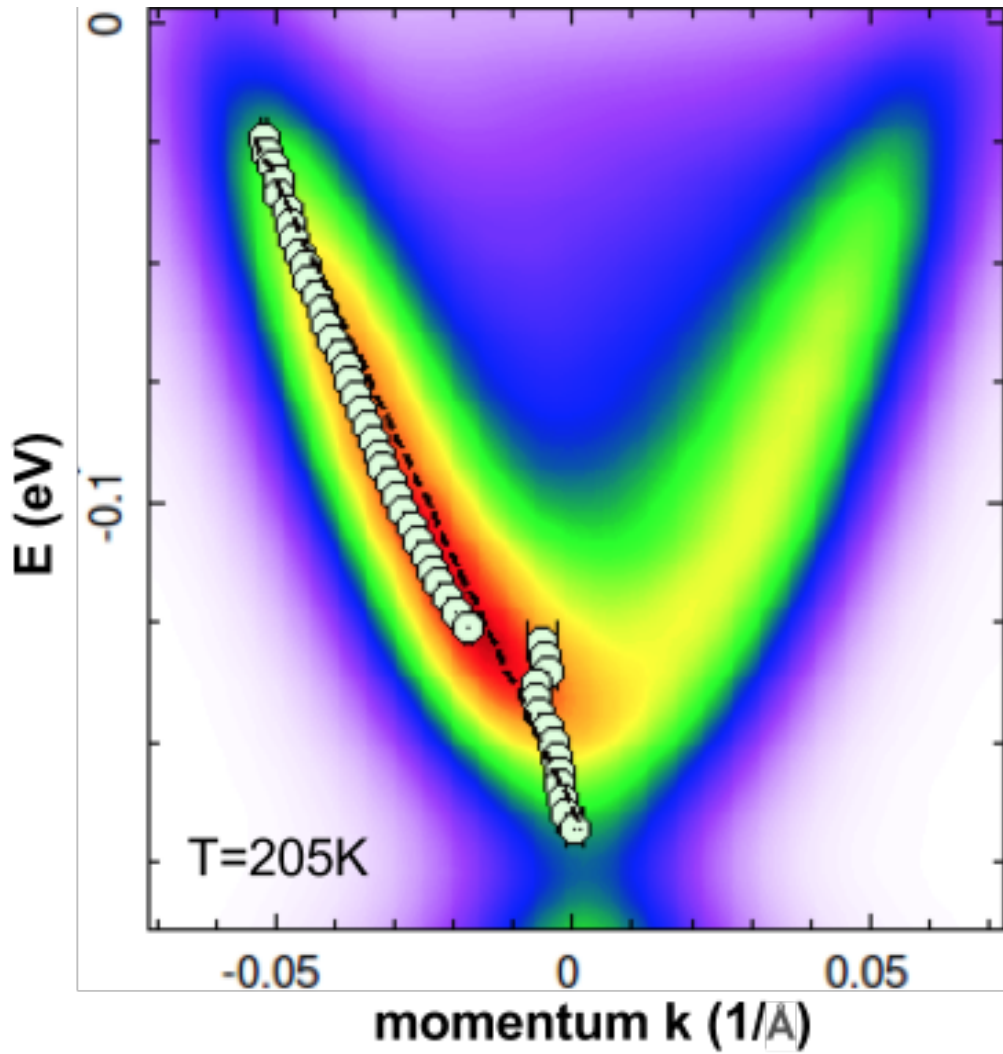
Figure 18: Plot of a linear fit to the MDC peak positions of the entire linear and parabolic left arm of the gamma point scan at T=205K. The peak positions breaks its linear behavior at around E=-0.130 eV; the fit line, in black, deviates to a lower slope magnitude than for a purely linear region.
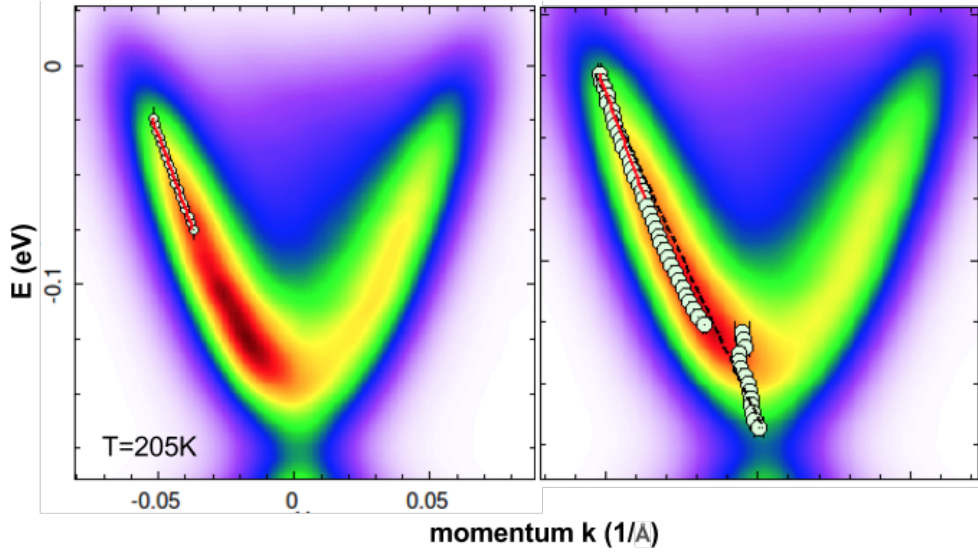
Figure 19: a) Plot of a linear fit to the MDC peak positions of only the linear low energy region of the gamma point scan at T=205K. The fit line, in red, displays a much closer fit to the data points. b) Overlay comparison of fit lines for entire region *black* and linear low E region only*red*. The actual data points for the MDC peak positions are in circles.

for Pan's determination for the same material, Bi_2Se_3, of $\lambda = 0.076$. The difference between Reichwein's original analysis and the one discussed here is consistent with the consistently lower Fermi velocities determined from this data set. The range of velocities determined were between 3.25 and 3.54, compared to Reichwein's range of 3.5 to 4.9. In comparison, the analysis done on the combined region results in a lower range of velocities between 2.50 and 3.09, and a lambda value of $\lambda = 0.158$. Interestingly, this value corresponds well to the Giraud and Egger theoretical value for a strong TI Bi_2Te_3, of $\lambda = 0.13$. [10]. Exclusion of the higher-E parabolic region results in the lower values of lambda calculated here, by Pan in 2012, and previously in 2014 by Reichwein.
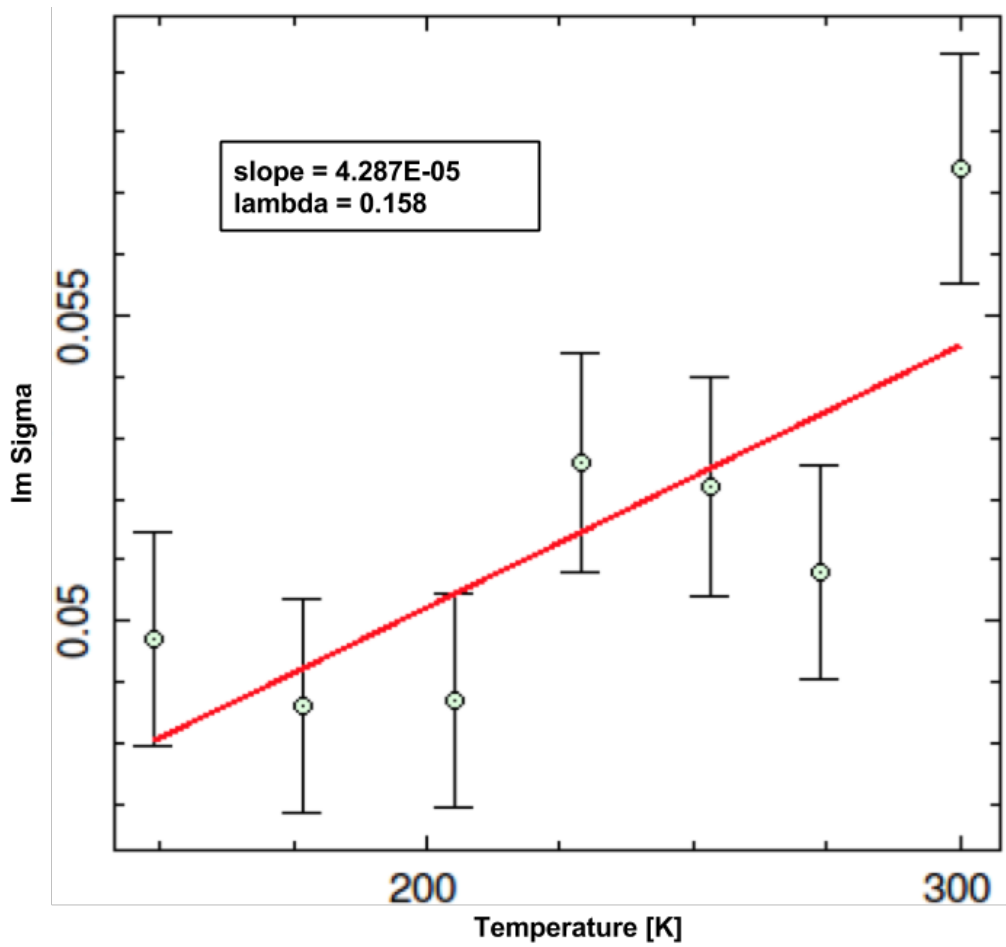
Figure 20: The coupling constant lambda is determined for the fits done for the combined linear and parabolic region analysis. $\lambda = 0.158 \pm 0.016$ is obtained to be compared to the linear-only analysis.
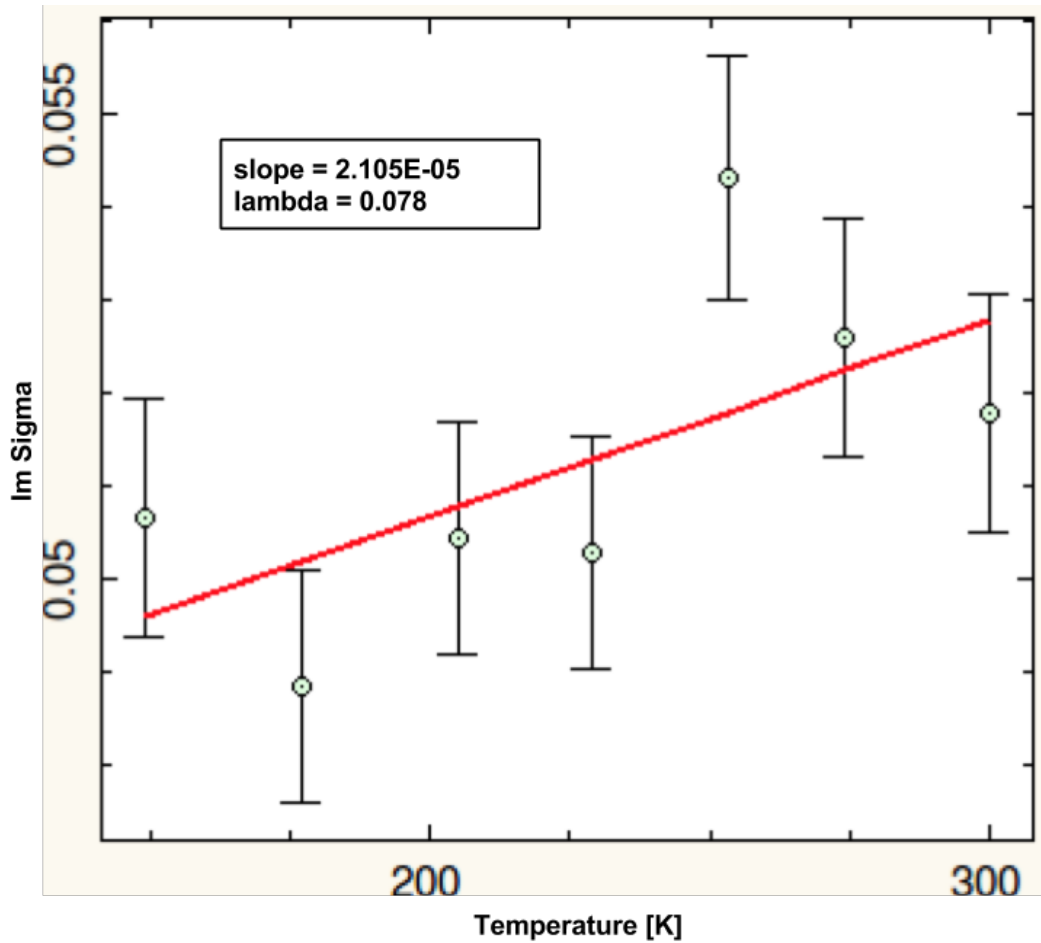
Figure 21: The coupling constant lambda is determined for the fits done for the properly cut linear-only region. $\lambda = 0.078 \pm 0.007$ is obtained, which is approximately half the value obtained from the combined region shown in Figure 20.

4 Future Work

Improvement in energy resolution for measurement could improve quantitative analysis of the effect of temperature broadening on the low obtained value of λ. As is, the low value of λ measured here and in previous studies is encouraging for the development of TBI in applications which require protected surface states, and benefit from surface states robust against small scattering interactions.

The best case explanation for the lack of observed effect from the adsorbates on surface state electron self-energy would be that the topological metallic states are protected from small surface potential disorders. This is the conclusion that Park et.al. tentatively suggest with their work on extracting Im? of Bi2Se3 from MDC and EDCs of ARPES spectra. However, they caution that it has been shown [4] that the type of adsorbate will have varying degrees of influence on the induced surface potential, and that this must be resolved before a conclusion on the protected nature of topological states from small induced potentials can be made.

For further work, a study where the type of adsorbate is monitored can be suggested. Because ARPES is conducted under high vacuum, introducing adsorbates within the vacuum environment would not be practical. A potential method would be to introduce low-coverage (0.1%) of controlled adsorbates to pristine samples. [4] Hydrogen doping, which is shown to change the Fermi surface area, has been shown to differ in its effect from doping with other gas or metal ion (NO2 or K, in the case of Bostwick). A variety of adsorbates should be tested, in addition to the work done quantifying the effect of doping density nH on the scale of Fermi surface distortion.

Manoharan group has shown, through construction of molecular graphene [11], that single molecule manipulation is a viable technique in the construction of

materials with deposited impurities, perhaps at specific lattice points. It can be suggested for future work that precise lattice doping of adsorbate atoms in a systematic study of lattice effects and localization would be illuminating toward next steps in experimental characterization of correlated materials.

5   Conclusion

Temperature dependence and aging effects on the surface of high-quality (low-Dirac point) crystals of Bi_2Se_3 were done with ARPES intensity data, examining the effect of different photon energies to minimize the presence of the bulk band in the spectra. The dispersion relations linear and parabolic regions were also examined, and the effect of a Gaussian convolution on EDC fit improvement was measured. EDC and MDC fits were done on optimized spectra, and the coupling constant λ was calculated to relatively quantify the strength of quasiparticle interactions.

Intra-surface interactions were observed to be a dominant effect in the higher self-energy range, through comparisons between the Lorentzian-based MDC fits and the Gaussian-convoluted FLS theory-based EDC fits. Our calculated value of $\lambda = 0.049 \pm 0.007$ is relatively weak compared to presently published values on this material. In addition, no expected spike was seen in self-energy near E_F, indicating some protection of surface states from surface-phonon and impurity scattering. The low value of λ measured here and in other work, in addition to the observation of surface state protection against lattice and impurity interaction potentials is a positive factor in implementing TBI in applications using spin-current or quantum well effects in a higher temperature, lower applied field setting than is currently needed to observe these characteristics. Development of a theory which formally includes electron-phonon coupling compared to the present form of the FLS theory which only includes

electron-electron interactions would improve fits; however, the complexity of extremely correlated systems makes this a daunting feat in both theory and in practical application with presently available computational capacity.

References

[1] Yoichi Ando. Topological insulator materials. *Journal of the Physical Society of Japan*, 82(10):102001, 2013.

[2] Carl Neil Berglund and WE Spicer. Photoemission studies of copper and silver: theory. *Physical Review*, 136(4A):A1030, 1964.

[3] B Andrei Bernevig, Taylor L Hughes, and Shou-Cheng Zhang. Quantum spin hall effect and topological phase transition in hgte quantum wells. *Science*, 314(5806):1757–1761, 2006.

[4] Aaron Bostwick, Jessica L McChesney, Konstantin V Emtsev, Thomas Seyller, Karsten Horn, Stephen D Kevan, and Eli Rotenberg. Quasiparticle transformation during a metal-insulator transition in graphene. *Physical review letters*, 103(5):056404, 2009.

[5] Riccardo Comin and Andrea Damascelli. Arpes: A probe of electronic correlations. In *Strongly Correlated Systems*, pages 31–71. Springer, 2015.

[6] Andrea Damascelli. Probing the electronic structure of complex systems by arpes. *Physica Scripta*, 2004(T109):61, 2004.

[7] Andrea Damascelli, Zahid Hussain, and Zhi-Xun Shen. Angle-resolved photoemission studies of the cuprate superconductors. *Reviews of modern physics*, 75(2):473, 2003.

[8] A Einstein. Über einen die erzeugung und verwandlung des lichtes betreffenden heuristischen gesichtspunkt [adp 17, 132 (1905)]. *Annalen der Physik*, 14(S1):164–181, 2005.

[9] HY Fan. Theory of photoelectric emission from metals. *Physical Review*, 68(1-2):43, 1945.

[10] Sébastien Giraud and Reinhold Egger. Electron-phonon scattering in topological insulators. *Physical Review B*, 83(24):245322, 2011.

[11] Kenjiro K. Gomes, Warren Mar, Wonhee Ko, Francisco Guinea, and Hari C. Manoharan. Designer dirac fermions and topological phases in molecular graphene. *Nature*, 483(7389):306–310, 03 2012.

[12] G.-H. Gweon. *Angle resolved photoemission study of Fermi surfaces and single- particle excitations of quasi-low dimensional materials*. PhD thesis, University of Michigan, Ann Arbor, 1999.

[13] Heinrich Hertz. Ueber einen einfluss des ultravioletten lichtes auf die electrische entladung. *Annalen der Physik*, 267(8):983–1000, 1887.

[14] Adam Kaminski and Helen M Fretwell. On the extraction of the self-energy from angle-resolved photoemission spectroscopy. *New Journal of Physics*, 7(1):98, 2005.

[15] Charles L Kane and Eugene J Mele. Quantum spin hall effect in graphene. *Physical review letters*, 95(22):226801, 2005.

[16] YK Kato, RC Myers, AC Gossard, and DD Awschalom. Observation of the spin hall effect in semiconductors. *science*, 306(5703):1910–1913, 2004.

[17] Markus König, Steffen Wiedmann, Christoph Brüne, Andreas Roth, Hartmut Buhmann, Laurens W Molenkamp, Xiao-Liang Qi, and Shou-Cheng Zhang. Quantum spin hall insulator state in hgte quantum wells. *Science*, 318(5851):766–770, 2007.

[18] GD Mahan. Theory of photoemission in simple metals. *Physical Review B*, 2(11):4334, 1970.

[19] WL McMillan. Transition temperature of strong-coupled superconductors. *Physical Review*, 167(2):331, 1968.

[20] Joel E Moore. Topological insulators. *Spectrum, IEEE*, 48(7):38–57, 2011.

[21] Joel E Moore and Leon Balents. Topological invariants of time-reversal-invariant band structures. *Physical Review B*, 75(12):121306, 2007.

[22] Shuichi Murakami, Naoto Nagaosa, and Shou-Cheng Zhang. Spin-hall insulator. *Physical review letters*, 93(15):156804, 2004.

[23] Z-H Pan, AV Fedorov, D Gardner, YS Lee, S Chu, and T Valla. Measurement of an exceptionally weak electron-phonon coupling on the surface of the topological insulator bi 2 se 3 using angle-resolved photoemission spectroscopy. *Physical review letters*, 108(18):187001, 2012.

[24] SR Park, WS Jung, Chul Kim, DJ Song, C Kim, S Kimura, KD Lee, and N Hur. Quasiparticle scattering and the protected nature of the topological states in a parent topological insulator bi 2 se 3. *Physical Review B*, 81(4):041405, 2010.

[25] E. J. Reichwein. A complete analysis of the intrinsic properties of the topological states in bi2se3 by angle resolved photoemission spectroscopy. Master's thesis, University of California, Santa Cruz, 2014.

[26] Friedrich Reinert and Stefan Hüfner. Photoemission spectroscopy—from early days to recent applications. *New Journal of Physics*, 7(1):97, 2005.

[27] WE Spicer. Photoemissive, photoconductive, and optical absorption studies of alkali-antimony compounds. *Physical review*, 112(1):114, 1958.

[28] Göran Wendin. *Breakdown of one-electron pictures in photoelectron spectra.* Springer, 1981.